PAPER

Check for updates

Facile synthesized zinc oxide nanorod film humidity sensor based on variation in optical transmissivity†

Rajni Verma, [ID] ‡*[a] Saurabh Pathak, [ID] ‡[b] Kajal Kumar Dey, [ID] [c] Samiksha Sikarwar,[d] B. C. Yadav [ID] [d] and A. K. Srivastava [ID] *[e]

Variation in the transmitted light intensity from metal oxide thin films with moisture content provides a great opportunity to use them for humidity sensing. Herein, we have developed a novel and simple humidity sensor based on ZnO nanorod (ZNR) thin films which work as transmission-based sensing elements in an in-house fabricated sensing setup. The ZNR sensing element shows excellent linear sensing performance in the relative humidity (RH) range 10–90% and does not show any hysteresis. A maximum change in optical power of ~95 µW is observed with the change in RH in the range 10–90%, for the sample with the smallest crystallite size (ZNR1) and highest pore diameter of the ZNR film. Also, a maximum sensitivity of 1.104 µW/% RH is observed for the ZNR1 sample which drops to 0.604 µW/% RH for the highest crystallite size sample (ZNR4). The presence of oxygen vacancies and the micro-porous nature of the film allow the absorption of water vapour on the film which deflects light at different angles that vary with the moisture content. The experimental results suggest that the ZNR film with a smaller crystallite size and larger pore diameter is more sensitive for humidity measurements. Further, an improved sensing performance is perceived in ZNRs because of the larger surface area of the nanorods. The ZNR based sensing elements do not suffer from ageing effects and exhibit high repeatability (88.74%). Further, the humidity sensor has a response time of 62 seconds and recovery time of 100 seconds which can be considered as a fairly quick response.

1 Introduction

The stipulation for monitoring/controlling the ambient environment (temperature, atmospheric pressure and humidity) for balancing the microclimate surroundings in museums, organic farming, paper industry, sophisticated instruments, pharmaceuticals, electronics manufacturing, packaging, research laboratories, the medical industry, and standard/calibration labs has led to the development of novel and advanced sensing techniques.[1–4] Humidity is a widespread measured quantity that plays a very significant role in diverse fields of applications from small-scale domestic applications to large-scale industrial processing.[5–7] It is a physical quantity which quantifies the content of water vapour in the air or any other gases and is generally measured in terms of absolute humidity, dew point, and relative humidity.[8,9] Humidity sensing and control has attracted tremendous attention as water vapour tends to condense or evaporate at the surface with the slightest change in surrounding temperature.[10,11] Water vapour is composed of highly reactive dipolar molecules, due to the difference in electronegativity of oxygen and hydrogen atoms which changes with minute variations in surroundings, making accurate sensing and control key for industrial and scientific applications.[12,13] Also, the accurate control and measurement of humidity plays a key role in triggering different chemical processes and optimizing device performance and ergonomics, making precise measurement of humidity important.[14–16] Maintaining the humidity level is not only challenging but also intricate in many cases such as in highly sophisticated instruments, pharmaceutical processing, respiratory equipment, biological products and in agriculture.[17,18]

Humidity sensors have been developed based on numerous mechanisms such as optical, electrical, mechanical, thermal (conductivity), electronic (ionic or resistive) or acoustic.[19] All these techniques possess certain pros and cons for different application areas.[7,20–23] Nowadays, many novel mechanisms based on the optical and optoelectronic properties of materials

[a]*School of Physics, The University of Melbourne, Parkville, VIC 3010, Australia. E-mail: rajni.verma@unimelb.edu.au*

[b]*Department of Mechanical Engineering, The University of Melbourne, Parkville, Victoria 3010, Australia*

[c]*Centre for Nanoscience & Technology, Prof. Rajendra Singh Institute of Physical Sciences for Study and Research, VBS Purvanchal University, Jaunpur, Uttar Pradesh 2220003, India*

[d]*Department of Physics, School of Physical and Decision Sciences, Babasaheb Bhimrao Ambedkar University, Lucknow 226025, India*

[e]*CSIR-Advanced Materials and Processes Research Institute, Bhopal, Madhya Pradesh 462026, India. E-mail: director@ampri.res.in*

† Electronic supplementary information (ESI) available. See https://doi.org/10.1039/d1na00893e

‡ These authors contributed equally.

are also gaining significant interest.[8,24] These types of humidity sensors are characterized by their high sensitivity, remote analysis capabilities and electromagnetic radiation free monitoring. In this method, sensing is performed based on the modulation of various optical characteristics like transmitted light intensity, refractive index, wavelength modulation and frequency shift.[8,25] They do not suffer any perturbation in the measurement of humidity due to the interference from nearby electric and magnetic fields which is one of the major advantages of optical humidity sensors.[24,26,27]

The primary sensing material groups used for humidity sensing are ceramics, organic polymers, and resistive polyelectrolytes.[8,13,28] Ceramic sensors show good stability even under a highly humid atmosphere and are usually highly sensitive, possess rapid response time, excellent reproducibility, and a wide measurement range. Among the ceramics, metal oxides have been extensively employed for humidity sensing due to their high stability, ease of synthesis and good chemical stability.[11,29-32] A wide variety of metal oxides such as ferrites (AB_2O_4, where A = Ni, Zn, Sr, Co, *etc.* and B = Fe, Gd, Ti, *etc.*), $BaTiO_3$, $Li_2B_4O_7$, $MgCr_2O_4$, $BaTiO_3$, SiO_2, In_2O_3, TiO_2, ZnO, SnO_2, Al_2O_3, *etc.* have proved to be very popular materials for humidity sensing based on the change in impedance with relative humidity (RH) variation.[25,33-35] However, some of them do have drawbacks in the form of poor recovery that requires subsequent heating for reuse.[36,37] A significant effort has been made in these materials to obtain improvement in linearity and sensitivity by adopting nanostructuring approaches. Recent trends in these materials suggest that they have the potential to be used for a wide range of applications with good sensitivity with different mechanisms which makes them the most desirable materials for humidity sensing.[38-40] Humidity sensing using nanostructured materials as sensing elements has also attracted considerable attention in the recent past.[41,42] A vast number of novel advanced functional metal oxide nanomaterials have been probed for the design and development of highly sensitive and efficient humidity sensors.[1,29,30,33-35,43]

Various morphologies of metal oxide nanomaterials such as nanoparticles,[27] nanorods,[30] nanowires,[44] nanoflowers[34,45] and nanotubes[46] have displayed excellent humidity sensing properties. Humidity sensors based on these nanomaterials with different morphologies have been probed extensively due to their excellent optical and electrical properties.[31,47] ZnO nanomaterials have shown great potential for a variety of sensors due to their superior opto-electronic properties.[48] Their highly surface active optical and opto-electronic properties with selective response to particular gases make them ideal candidates in terms of humidity and gas sensing properties.[29] ZnO nanoparticles showed high reactivity towards different gases such as CO, CH_4 and H_2.[49] They also have good reactivity with benzene and volatile organic liquids such as ethanol and acetone, which is why they have become a very desirable material for the sensing element. However, a very limited number of investigations have been performed on the humidity sensing of ZnO nanomaterials with varying morphologies employing optical sensing methods. Only a few reports in the literature have utilized ZnO nanomaterials as sensing elements

in optical mechanism-based humidity sensors and none have investigated ZNRs for humidity sensing using this mechanism.

In this work, we have designed a unique humidity sensor based on the optical mechanism in which the change in transmitted light intensity through the sensing element has been capitalized for the humidity measurement. A facile sol–gel synthesis method has been adopted for the synthesis of ZNRs with different sizes. An in-house experimental setup is developed consisting of a He–Ne laser, beam expander/condenser, hygrometer, optical detector, and moisture-controlled environment chamber (M-CEC). The sensing element has been fabricated by spin coating the ZNRs on a glass substrate and placed on the exit of the M-CEC. The change in RH of the M-CEC is achieved in the range 10–90% and the corresponding change in laser light intensity due to physisorption and chemisorption on the surface of the ZNR film is measured using an optical meter. The change in the value of optical power with RH can be quantified for the development of absolute RH measurement. The structure and morphology of the ZNRs have been identified by X-ray diffraction (XRD) and transmission electron microscopy (TEM). Further, the oxygen vacancies in the ZNRs play a critical role in sensing element performance which is probed by photoluminescence measurement. Also, the porosity and pore diameter significantly affect the physisorption and chemisorption processes and they are calculated using the Brunauer–Emmett–Teller (BET) method.

2 Experimental details

2.1 Synthesis of ZnO nanorods (ZNRs) and fabrication of the sensing element film

Zinc acetate dihydrate ($Zn(CH_3COOH)_2 \cdot 2H_2O$, LR, 98%, Thomas Baker Pvt. Ltd, India), absolute ethanol (C_2H_6O, AR, 99.9%, SD Fine-Chem Ltd, India) and polyvinyl alcohol (PVA, LR, 75%, Central Drug House Pvt. Ltd, India) were procured for the synthesis of ZNRs. Double distilled (DI) water (Millipore (18 MΩ)) was used throughout the entire experimentation.

The ZNR thin film sensing element was fabricated by a facile two-step method. In the first step, ZNRs were synthesized by the sol–gel method followed by thin film fabrication using rotation-controlled spin coating in the second step. For ZNR synthesis, 0.3 M zinc acetate dihydrate (precursor) and 3 g of PVA were mixed with solvents (water and ethanol) under constant stirring for 30 minutes at 60 °C to obtain a homogeneous solution. PVA was added to the solution to propagate the directional growth and it also works as a capping agent. The temperature of the solution was increased to 90 °C and kept constant for 30 minutes to convert the obtained sol into a gel (gelation: the resultant solution becomes a viscous gel which turns opaque). The produced gel was then dried and calcined at 400 °C for 4 hours to increase the crystallinity of ZNRs. Four different samples were prepared by varying the solvent compositions (ratio of water and ethanol). The solvent composition of ethanol : water was varied from pure ethanol (ZNR1) to 30 : 70 (ZNR2), 70 : 30 (ZNR3) and pure water (ZNR4). The controlled microstructure and uniformity of the film deposition were obtained by optimizing various deposition parameters such as
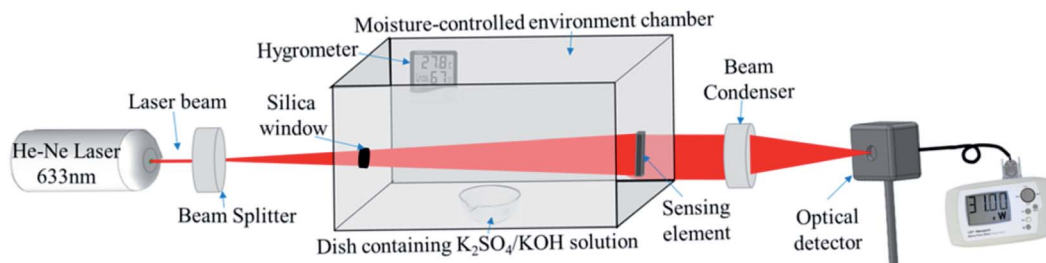
Fig. 1 Schematic of the experimental setup developed in-house for humidity sensing measurements. Adopted from ref. 8.

rotation speed during spin coating, solution density and viscosity.[48,50–52]

Films were deposited on the borosilicate substrate with dimensions of 1.5×1.5 cm^2. Prior to the deposition, the glass substrates were cleaned using an ultrasonic cleaner (WUC-AO2H) by dipping them in a solution of DI water and isopropyl alcohol. The cleaned glass substrates were vacuum dried at 100 °C for 15 minutes. ZNRs were deposited on these substrates using a photoresist spinner (METREX RC100, India) at a speed of 3000 rpm followed by drying for 15 minutes at 60 °C on a hot plate (AMBASSADOR, India). Thus, the obtained films with high uniformity were used as sensing elements in optical humidity sensing measurement.[8,27]

2.2 Characterization techniques

The crystallinity, phase and structure of the ZNR samples were studied by XRD patterns obtained using a Rigaku (Ultima-IV) X-ray diffractometer equipped with a monochromatic Cu Kα radiation ($\lambda = 1.541$ Å) X-ray source. Further, the crystallite sizes of the ZNRs were calculated by the Debye–Scherrer and Williamson–Hall (W–H) methods. Moreover, to confirm the nanorod formation and to investigate the morphology of the prepared samples, a scanning electron microscope (Zeiss EVO MA-10 SEM operating at 10 keV) was used. Further, the microstructural characteristics, lattice fringe spacing and selected area electron diffraction (SAED) were studied using a high-resolution transmission electron microscope (FEI Tecnai G2 F30 STWIN HRTEM operating at an accelerating voltage of 300 kV). The specific surface area and pore size distribution of samples were obtained from a N$_2$ adsorption/desorption analysis performed at 77 K on a BELmax 00126 system *via* BET characterisation. Finally, the room temperature emission properties of the ZNR samples were probed using a photoluminescence (PL) spectrophotometer (FL-1039, HORIBA Jobin Yvon, USA).

2.3 Description of the sensing set-up

The optical humidity sensing set-up is based on the principle of variation of the transmitted light intensity. The schematic of the experimental set up is shown in Fig. 1 which shows various components of the system such as a 2 mW He–Ne LASER (Research Electro Optics Inc. 30989), diverging lens (10× magnification), humidity control chamber, sensing element, beam condenser and optical power meter (Newport 1916-R).

The experimental setup is kept on a vibration-free optical table (Newport M-RS2000-48-8) to avoid any variation caused by the external perturbations. A 2 mW laser beam with 633 nm wavelength was incident on diverging lens of 10× magnification which expands the beam to cover the complete surface of the sensing film. An M-CEC is fabricated in-house with transparent glass windows which contain a hygrometer and humidifier/dehumidifier to effectively control and monitor the RH (in the range 10–90%) of the chamber. The humidity inside the M-CEC is controlled by a dish containing a saturated solution of K$_2$SO$_4$/KOH (Fisher Scientific) in DI water which works as a humidifier/dehumidifier. The ZNR based sensing elements were adjusted in such a way that they perfectly aligned perpendicular to the incident beam so that the beam should pass through the maximum surface area of the sensing element. Further, the laser beam was converged using a beam condenser to achieve point focus on the optical power meter which maximizes the impinging light intensity. The optical meter is attached to the optical table in such a way that the condensed beam could impinge on the centre of the optical meter to avoid any intensity loss. The sensing set-up should not be disturbed during measurement because the measurement setup is highly sensitive and even the slightest changes in the angle of incidence of the incident beam may result in a significant change in the transmittance through the film.[8,24]

3 Results and discussion

3.1 Phase identification by XRD

The XRD patterns of all the ZNR powder samples are shown in Fig. 2. All the samples (ZNR1, ZNR2, ZNR3 and ZNR4) exhibit the wurtzite phase (hexagonal) of ZnO (space group $P6_3mc$) with lattice parameters $a = b = 0.325$ nm, $c = 0.520$ nm. The sharp peaks obtained for all the samples indicate high crystallinity in the samples. The diffraction peaks corresponding to Bragg diffraction angle (2θ) values of 31.81°, 34.57°, 36.36°, 47.66°, 56.67°, 62.87°, 66.45°, 67.9°, 69.1°, 72.65° and 77.05° for the ZNR1 sample correspond to the (100), (002), (101), (102), (110), (103), (200), (112), (201), (004) and (202) planes respectively (JCPDS no. 36-1451).[48,50,51,53] Similarly, all the other ZNR samples also possess 2θ values in near proximity which confirms that all the samples have a highly crystalline wurtzite phase. No additional peak was observed in any of the samples which confirms the phase purity of the prepared samples. Further, to calculate the crystallite size of each sample, XRD patterns were fitted to
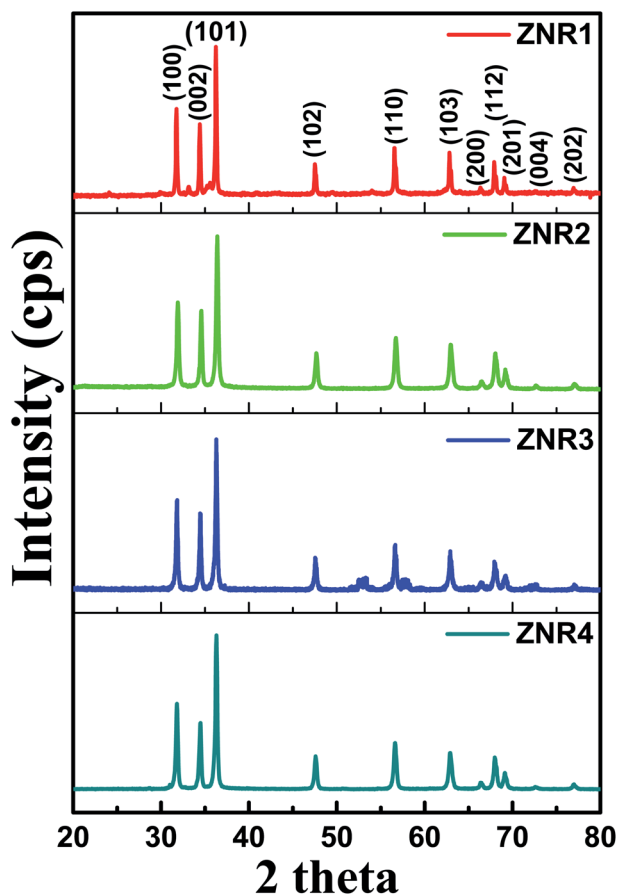
Fig. 2 XRD patterns of ZnO nanorod (ZNR1, ZNR2, ZNR3 and ZNR4) samples with indexed diffraction peaks corresponding to the standard JCPDS data card (36-1451).

calculate the full width at half maxima (FWHM) and Bragg diffraction angle. The average size of an individual crystallite was estimated using the Debye–Scherrer equation: [54–56] $D = \dfrac{k\lambda}{\beta \cos \theta}$, where D is the crystallite size, k is the Scherrer constant, and λ is the X-ray wavelength ($\lambda = 1.5406$ Å). Average crystallite sizes of the particles were calculated by averaging crystallite sizes corresponding to the most intense peaks found in the respective XRD patterns (101). The crystallite sizes obtained for samples ZNR1, ZNR2, ZNR3 and ZNR4 are 29.0, 33.8, 29.6 and 39.7 nm, respectively as shown in Table 1.

The variation in the crystallite sizes suggests that the solvent composition plays a key role in controlling the rod shape and size of the ZnO nanomaterials. Furthermore, the Debye–

Scherrer equation does not take into account the instrumental and strain broadening of the diffraction peak which results in miscalculation of the crystallite size values. To solve this issue, we have employed the W–H method to verify the crystallite size values obtained by the Debye–Scherrer method. The W–H method accounts for the peak broadening that can be expressed in terms of microstrain broadening factor elaborated by the equation $\beta_{hkl} \cos \theta = 4\varepsilon \sin \theta + \dfrac{k\lambda}{D}$, where $4\varepsilon \sin \theta$ is the strain factor.[22,57–60] Fig. 3 shows the W–H plot obtained for all the samples by fitting the $4 \sin \theta$ and $\beta \cos \theta$ plot. The slope and intercept obtained by plotting a graph between $4 \sin \theta$ and $\beta \cos \theta$ provide information about the average crystallite size and induced strain, respectively.[53,60–63] The values of the strain and crystallite size obtained by W–H plots are provided in Table 1. The average crystallite size calculated by the W–H method varies from 33.50 to 47.09 nm and by the Scherrer method, it varies from 29.0 to 39.7 nm. The values of the crystallite size obtained by both Debye–Scherrer and W–H methods are in good agreement with each other. The 2θ values for all the samples, ZNR1, ZNR2, ZNR3 and ZNR4, were found to be the same, however, the peak intensity varies due to difference in crystallinity.

3.2 Structural investigations by electron microscopy

The surface morphological and structural information of the as-prepared ZnO samples was investigated by electron microscopy techniques. All four samples reveal the rod-like morphology of ZnO with different aspect ratios (length/width). It is evident from the SEM micrographs (Fig. 4a–d) that solvent composition plays a significant role in nucleation followed by growth of nanorods in different orientations.[51,64] This results in varied length and diameter of ZNRs. To obtain further insights regarding structural information and to calculate the length and width of the obtained nanorods, HRTEM was performed. The ZNR1 sample, where pure ethanol was added as solvent, was found to exhibit the lowest aspect ratio among the four samples. Meanwhile, the aspect ratio of the ZNR4 sample, where pure aqueous solution was used, was observed to be the highest amongst all the samples i.e. 9.4 (length 404 nm and diameter 43 nm). From the bright field image of the ZNR1 sample (Fig. 4e), the length is elucidated to be 269 nm and the diameter 77 nm. The calculated aspect ratio is ~3.5 for ZNR1. Bright field images of samples ZNR2, ZNR3 and ZNR4 (Fig. 4g, i and m) depict high agglomerated rods few microns in length. Overall, the aspect ratios of these nanorods were found to be in the range of 3.1 to 9.4. HRTEM micrographs of samples ZNR1,

Table 1 Crystallite size (Scherrer method and W–H plot), aspect ratio, pore diameter and sensitivity of the ZNR based sensing element

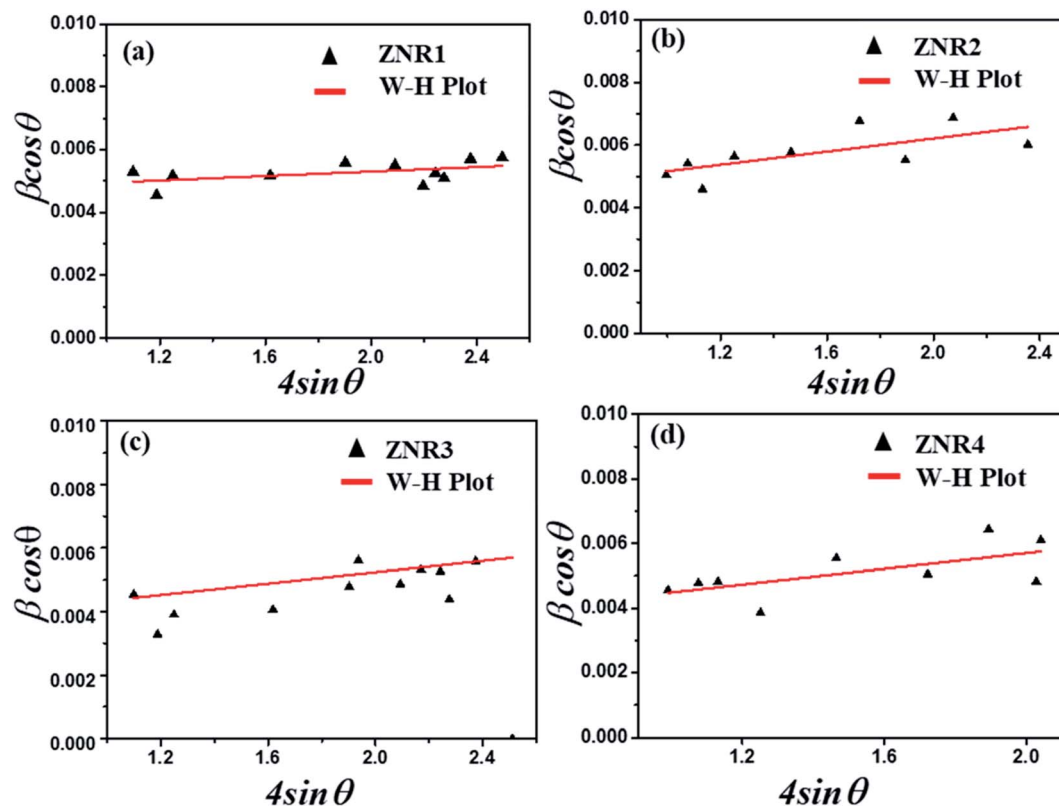| Samples	Solvent composition (ethanol : water)	D, Scherrer method (nm)	Intercept	Slope (strain)	D, W–H method (nm)	Aspect ratio (l/d)	Pore diameter (nm)	Sensitivity
ZNR1	100 : 0	29.0	0.00459	0.000357	33.50	269/77 = 3.5	39.93	1.14
ZNR2	30 : 70	33.8	0.00345	0.000894	44.60	145/30 = 4.8	—	0.94
ZNR3	70 : 30	29.6	0.00412	0.00105	37.30	117/29 = 4.0	—	1.07
ZNR4	0 : 100	39.7	0.00327	0.00122	47.09	404/43 = 9.4	35.58	0.62

Fig. 3 W−H plots of ZnO nanorod samples (a) ZNR1, (b) ZNR2, (c) ZNR3 and (d) ZNR4.

ZNR2, ZNR3 and ZNR4 (Fig. 4f, h, j and l) demonstrate a clear regular interplanar distance of 0.25 and 0.28 nm that corresponds to the (101) and (100) lattice planes respectively indicating that the nanorods have good crystallinity and no significant imperfections or defects. The SAED pattern shows bright spots (Fig. 4k) ascribed to the polycrystalline nature of the obtained ZNRs. The (103) and (201) planes confirm the formation of ZnO.[64]

3.3 Humidity sensing measurements

The room temperature humidity sensing measurements on the ZNR samples were performed within the RH range of 10–90%. Fig. 5a–d show the humidity response on the transmitted light intensity observed at the optical power meter. From this figure, it is evident that the transmitted light intensity decreases with the increase in RH which can be quantified for the measurement of absolute humidity. All the ZNR samples show almost linear behaviour with significant change in optical power with change in RH. The measurements were performed in both increasing (10–90%) and decreasing (90–10%) modes. Almost similar changes in optical power values were perceived for all the samples in both increasing and decreasing modes which suggests that the sensing element does not suffer from any hysteresis. From Fig. 5a, it is evident that the change in optical power is more drastic in the ZNR1 samples where a 90 μW change is observed for the change in RH from 10 to 90%. The corresponding change for other ZNR samples is 85, 75 and 50

μW for samples ZNR2, ZNR3 and ZNR4, respectively with the change in RH 10–90%. For the ZNR1 sample, good linear power output characteristics were obtained with a small deviation (flattening) at lower RH as evident from Fig. S1† which shows the R-square values of the fitting in the range 0.95–0.99.[65] This flattening at lower RH can be correlated with the hysteresis of the sensing element as the sensing element retains some of the memory of the past and does not reach its original state (Fig. 5a). ZNR2 samples do not exhibit any flattening at lower RH and show good linear output (Fig. S1†); however, a small plateau at very high RH values was observed which corresponds to capillary condensation (Fig. 5b). Further, ZNR3 shows similar behaviour to ZNR1 and a small amount of flattening is observed at lower RH. The crystallite size and aspect ratio of ZNR1 and ZNR3 samples are similar which is the primary reason for achieving the same characteristics; however, the power output in ZNR3 samples is slightly lower compared to that in ZNR1 samples. Finally, ZNR4 samples have the lowest power output corresponding to the RH change from 10 to 90%. Also, a flattening in the power output curve at higher RH due to capillary condensation, similar to the one in ZNR2, is observed here (Fig. 5d). Compared to the rest of the samples, the linearity of the ZNR4 samples in the middle range is also substandard.

Sensitivity is one of the most important parameters for a material for its application as a sensor. Sensitivity is generally defined as the "change in input required to generate a unit change in output".[66] For the output response for a sensor, the sensitivity can be calculated from the slope of the curve in which the output
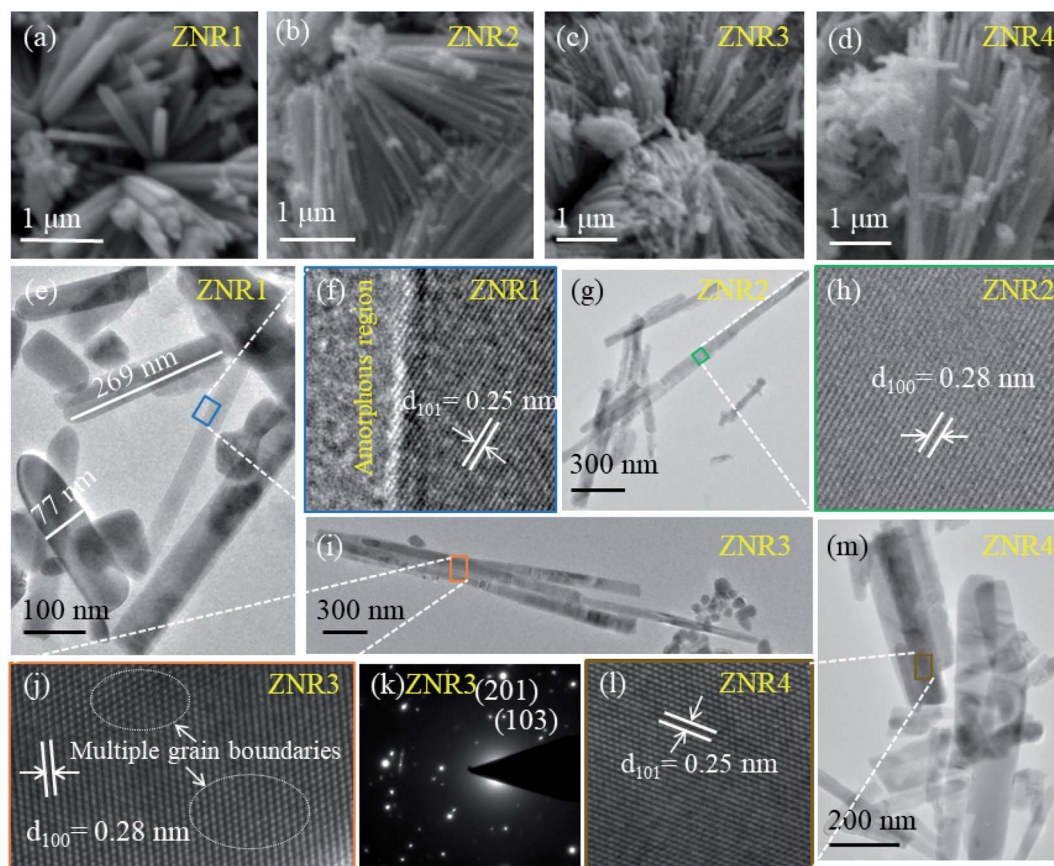
Fig. 4 Electron microscopy images of ZnO nanorods. (a–d) SEM images, and (e, g, i and m) bright-field and (f, h, j and l) high-resolution TEM images of samples ZNR1, ZNR2, ZNR3 and ZNR4, respectively. (k) SAED pattern of the ZNR3 sample.

response is linear. For the present case, the humidity *vs.* power output characteristics are almost linear and thus the sensitivity is calculated for the entire range of % RH using the following formula:

$$\text{Sensitivity } (S) = \frac{\text{change in transmitted power}}{\text{corresponding change in \% RH}}$$

$$= \frac{\Delta I_t}{\% \ \Delta RH} \mu \frac{W}{\% \ RH},$$ where ΔI_t is the change in transmitted intensity of light and % ΔRH is the corresponding change in % RH.[8,24] Fig. 5a–d show a nearly linear decrement in transmitted light intensity with a corresponding increase in % RH; however, in the higher % RH region the rate of decrement becomes slower. The film of the material with minimum crystallite size (sample ZNR1) was found to be the most sensitive among all the films and the sensitivity goes on decreasing with an increase in the crystallite size of the sensing material. Average sensitivities of sensing elements ZNR1, ZNR2, ZNR3 and ZNR4 were found to be ~1.140, 1.079, 0.938 and 0.622 μW/% RH respectively. The sensitivity significantly depends on the physicochemical characteristics of the sensing element.

The humidity sensing mechanism is based on the adsorption/desorption of water molecules by the pores of the sensor and subsequent capillary condensation in ZNRs as depicted in Fig. 6. The adsorbent and the adsorbate can interact either *via* physisorption or *via* chemisorption.[46] In the present study, ZNRs function as the adsorbent and moisture as the adsorbate. Physisorption is characterized by weak van der Waals forces, reversibility and formation of multiple layers of adsorbates on the adsorbent. However, chemisorption results in strong chemical bonding between them as observed in the present study.[8] The ionic zinc moiety, Zn^{2+}, interacts with OH^- of the water molecule resulting in strong chemical bonding which helps water molecules to get adsorbed inside the pores of ZNRs. Initially the pores on the surface of ZnO film are free from water molecules. When the humidifier is kept inside the chamber, % RH inside the chamber increases.

At low humidity (10–40% RH), the adsorption of water vapour inside the pores of the film takes place rapidly. The highly electropositive nature of the metal ion (Zn^+) in its oxide attracts the electronegative part (OH^-) of the water molecule and forms a strong chemical bond (Zn–OH) with the release of a proton (H^+). This leads to the bending of light after transmission as the refractive index increases. With exposure to humidity, % RH and hence adsorption of water molecules increases. In the medium humidity region (40–70% RH), adsorption takes place at the surface as well as on the walls of the pores' capillary releasing more H^+ ions and causing more bending of light. Lastly, in the high humidity region (70–90% RH), the water vapor condenses and forms a meniscus inside the pores of the film releasing hydronium ions (H_3O^+). In this region, the greatest bending of light takes place leading to a very
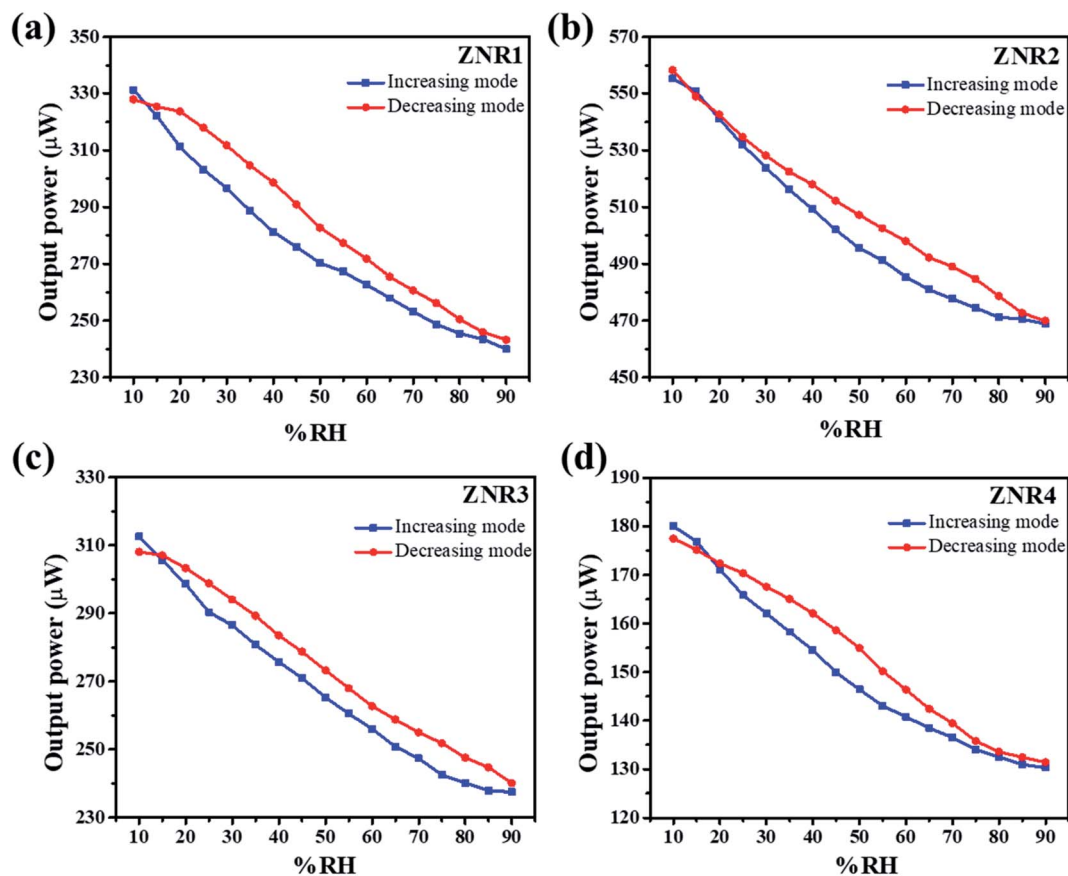
Fig. 5 Variation of output power with % RH showing the linear decrease in output power with a corresponding increase in % RH for (a) ZNR1, (b) ZNR2, (c) ZNR3 and (d) ZNR4.
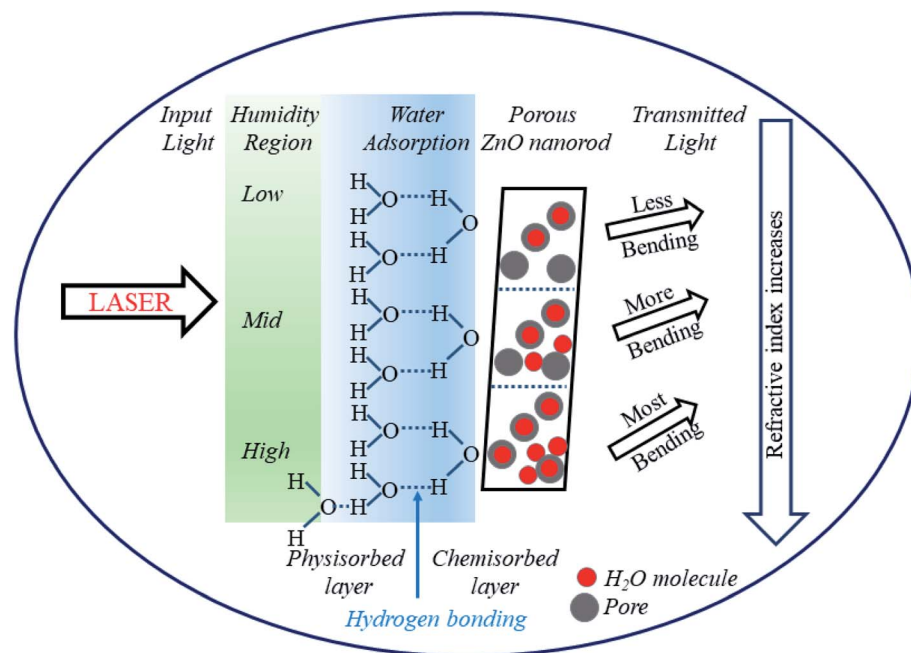

Fig. 6 Schematic of the sensing mechanism showing a decrease in output power with an increase in % RH for ZnO nanorods.

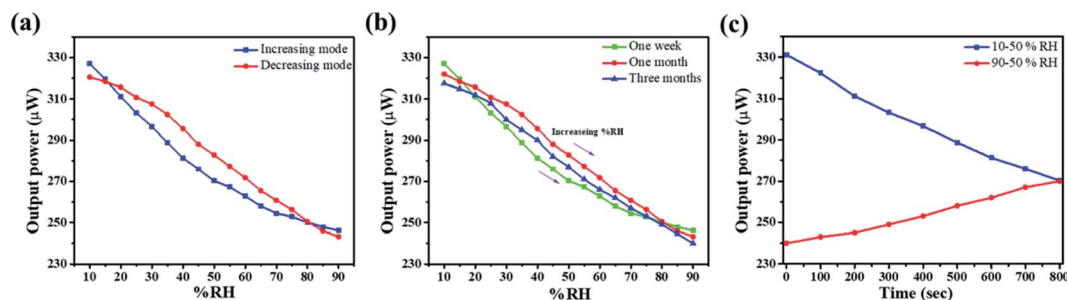© 2022 The Author(s). Published by the Royal Society of Chemistry

Fig. 7 Humidity measurement for investigating (a) repeatability, (b) aging effect with increasing % RH value from 10 to 90 and (c) response and recovery times of ZNR1.

small power output. Thus, it can be observed that the increase in % RH not only increases conductivity but also causes a change in refractive index.[25] Experimental curves show a linear decrement in output power with a corresponding increment in % RH. This decrement is due to a couple of factors: (i) as the % RH increases, condensation of water molecules inside the pores increases resulting in an increase in the thickness of the film. This further increases the absorption of light inside the material. Thus, the transmittance from the film decreases, and (ii) with the increase in % RH, charged ions in the form of H_3O^+ increase which condenses in the form of water inside the pores. This further leads to an increase in refractive index and hence bending of light, which results in a decrease of output power at the detector.[8]

The material with minimum crystallite size is the most sensitive among all the sensing elements. Therefore, all the sensing parameters such as repeatability, ageing and hysteresis have been checked for the ZNR1 sample only. Repeatability is one of the most important parameters of a sensor. For this investigation, the same experiment was repeated several times for ZNR1. Repeatability is the ability of an experiment to be duplicated, under the same conditions, by the same operator working with the same instruments. Fig. 7a shows the repeatability curve of ZNR1 which was obtained by taking the average of 10 measurements in increasing and decreasing modes. The sensitivity observed in this case is 1.011 μW/% RH, reflecting 88.74% repeatability of the sensing element. Further, the aging effect is also an important parameter. The experiment was repeated after one week, one month and three months with increasing % RH from 10 to 90 under the same experimental conditions. The respective curves have been plotted in Fig. 7b, where green, red and blue curves respectively show the humidity sensing performance after one week, one month and three months, respectively. From the curves, it can be observed that the material is quite stable in terms of its sensing

performance and is negligibly affected by its aging. Thus, the ZNR sensor is reproducible as well as stable and does not suffer from ageing. Sensors do not change the output state immediately on applying the input. Rather, it takes some time to attain the new output state. This particular period of time is called the response time, while the time needed to restore the response curve from the maximum to the first change in output value while repeating the experimental cycle in reverse order is defined as the recovery time.[39] The response time and recovery curve of the ZNR1 sample are shown in Fig. 7c from which it can be observed that the response and recovery times of the ZNR1 sensor are 62 s and 100 s, respectively.

3.4 Surface area determination by the BET method

To gain deep insight into the mechanism, the surface properties of ZNRs were examined by analyzing the results obtained from BET characterization. Samples with highest and lowest sensitivities were selected for in-depth analysis to determine the correlation between the humidity sensing performance and surface properties of the two samples. The surface area and pore volume of the samples were obtained using the nitrogen adsorption–desorption method. The calculated values of the surface area and pore volume of the ZNR1 and ZNR4 samples are shown in Table 2. Fig. 8a and c show the nitrogen adsorption–desorption isotherms of ZNRs. The volume adsorbed vs. relative pressure curve can be related to the type III adsorption isotherm (IUPAC classification) with a type III/IV hysteresis loop.[67] Fig. 8b and d show the BET plots of the ZNR1 and ZNR4 samples, respectively at 77 K. The specific surface area obtained from experimental results was found to be 7.43 m² g⁻¹ for ZNR4 which is higher than that of ZNR1 at 6.46 m² g⁻¹. However, the mean pore diameter for the ZNR1 sample was found to be higher than that of ZNR4. The mean pore diameter for the ZNR1 sample was determined using the slope and intercept obtained

Table 2 BET experimental results of samples ZNR1 and ZNR4

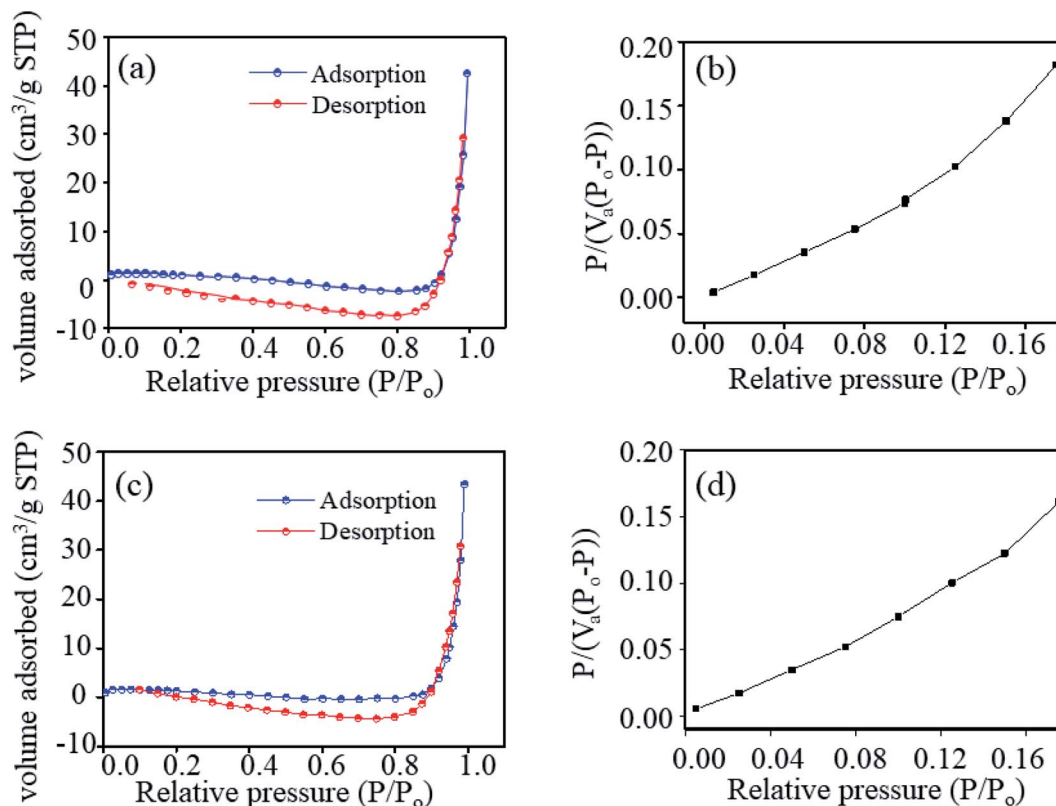| Sample	Slope	Intercept	Constant (C)	V_m: monolayer adsorption volume (cm³ g⁻¹)	Mean pore diameter (nm)	BET surface area (m² g⁻¹)
ZNR1	0.6731	7.39×10^{-4}	911.46	1.484	39.93	6.46
ZNR4	0.583	2.83×10^{-3}	206.69	1.707	35.58	7.43

Fig. 8 (a and c) Nitrogen adsorption−desorption isotherm and (b and d) BET plots of samples ZNR1 and ZNR4, respectively at 77 K.

experimentally and calculated to be 39.93 nm and that for ZNR4 was 35.58 nm. The higher pore diameter of ZNR1 corresponds to the improved sensing capability of this sample compared to that of the ZNR4 sample with a smaller pore diameter. Greater pore diameter provides more active sites for water adsorption and thus results in higher sensing capabilities as already explained in Section 3.3. So, we can conclude from the BET characterization that the higher pore diameter plays a critical role in enhancing the sensing performance of ZNR samples.

3.5 Determination of the optical properties of ZNRs using photoluminescence spectroscopy

The optical properties of ZNRs were obtained by analysing the emission spectra as shown in Fig. 9. All four samples, ZNR1, ZNR2, ZNR3 and ZNR4, show peaks at approximately 430 and 470 nm at an excitation wavelength of 330 nm. Although the position of the peaks is the same in all the samples, the peaks are not prominent in ZNR2 samples. Moreover, different samples have different PL intensities and the ZNR1 sample shows significantly higher PL intensity as compared to the other samples. The appearance of a violet-blue emission peak at 430 nm (2.88 eV) corresponds to interstitial zinc ions (Zn_i) at the top of the valence band.[68] The emission peak at 470 nm (2.63 eV) originates from deep level emission that can be attributed to oxygen vacancies or interstitial zinc ions.[69] It is interesting to note that the intensity of emission peaks is observed to be
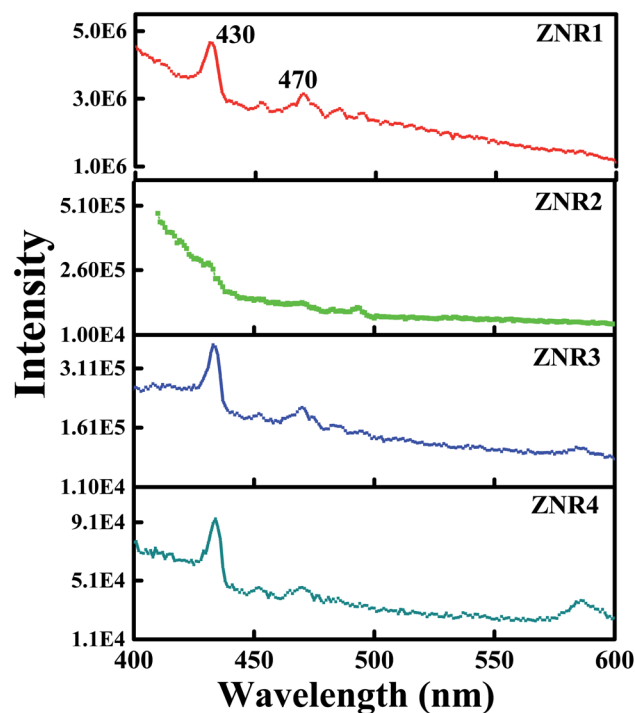

Fig. 9 PL spectra of all four samples (ZNR1, ZNR2, ZNR3 and ZNR4) of ZnO nanorods at an excitation wavelength of 330 nm.

© 2022 The Author(s). Published by the Royal Society of Chemistry

different for different samples due to the variation in crystallite size. An increase in nanocrystallite size leads to a decrease in PL intensity. As the crystallite size increases, the density of defects gets reduced followed by a decrease in surface to volume ratio.[42] Thus, the intensity of PL spectra is observed to be the lowest for the ZNR4 sample and highest for the ZNR1 sample. The existence of a higher number of defects in ZNR1 gives rise to more adsorption sites which is found to be in agreement with BET results. Further, we can conclude from the PL investigation that a smaller crystallite size results in more defect sites which results in higher sensitivity values.

4 Conclusion

Herein, we have demonstrated an optical humidity sensor which utilizes ZNRs as a sensing element and the change in transmitted light intensity of the incident laser beam passing through the sensing element has been quantified corresponding to the humidity change. The humidity works on a novel sensing mechanism in which the change in physicochemical properties of the ZNRs corresponding to the change in RH has been quantified for the development of a cost effective and simple humidity sensor. The humidity sensor shows excellent linear transfer function characteristics which makes it an appropriate selection for highly accurate and precise measurement. The ZNRs have been prepared through a facile and cost-effective chemical method and their corresponding films have been fabricated by spin coating. Microstructural characterization revealed the range of wurtzite phase ZNRs with varying rod lengths and aspect ratios. Further, the crystallite size obtained from the XRD patterns of the samples shows that the ZNR1 sample has the lowest while the ZNR4 sample has the highest crystallite size. The sensitivity of the ZNR1 and ZNR4 samples is 1.14 and 0.62 μW/% RH, respectively. This suggests that the lower crystallite size of the sensing elements provides better sensing performance. Further, the surface properties of the ZNR films significantly affect the sensing performance of the humidity sensor. The BET characterization of the samples confirms that greater pore diameter of the samples favours absorption of more water molecules on the film surface which results in a larger change in transmitted light intensity. The larger pore diameter in the ZNR1 sample provides more absorption sites and greater sensitivity compared to ZNR4 samples. Also, the PL investigation suggests that the smaller crystallite size is associated with more defect sites which may act as trapping centres for water molecules and improve the sensitivity of the ZNR sensing elements. Overall, from the humidity measurement and detailed materials property characterization we have established that the sensing element with smaller crystallite size and larger pore diameters provides better sensing performance. The sensor showed very high stability and 88.74% repeatability with low response and recovery times of 62 s and 100 s, respectively. Also, it does not suffer from ageing effects or hysteresis which makes it an ideal candidate for accurate and precise humidity measurement for remote sensing.

Conflicts of interest

There are no conflicts to declare.

Acknowledgements

References

1 N. Parvatikar, S. Jain, S. Khasim, M. Revansiddappa, S. V. Bhoraskar and M. V. N. A. Prasad, *Sens. Actuators, B*, 2006, **114**, 599–603.

2 L. Zhou, M. Wang, Z. Liu, J. Guan, T. Li and D. Zhang, *Sens. Actuators, B*, 2021, **344**, 130219.

3 K. Jain, R. P. Pant and S. T. Lakshmikumar, *Sens. Actuators, B*, 2006, **113**, 823–829.

4 Z. Duan, Y. Jiang, M. Yan, S. Wang, Z. Yuan, Q. Zhao, P. Sun, G. Xie, X. Du and H. Tai, *ACS Appl. Mater. Interfaces*, 2019, **11**, 21840–21849.

5 S. Jhulki, A. M. Evans, X.-L. Hao, M. W. Cooper, C. H. Feriante, J. Leisen, H. Li, D. Lam, M. C. Hersam, S. Barlow, J.-L. Brédas, W. R. Dichtel and S. R. Marder, *J. Am. Chem. Soc.*, 2020, **142**, 783–791.

6 Z.-H. Tang, W.-B. Zhu, J.-Z. Chen, Y.-Q. Li, P. Huang, K. Liao and S.-Y. Fu, *Nano Mater. Sci.*, 2021, DOI: **10.1016/j.nanoms.2021.11.006**.

7 S. Gbadamasi, M. Mohiuddin, V. Krishnamurthi, R. Verma, M. W. Khan, S. Pathak, K. Kalantar-Zadeh and N. Mahmood, *Chem. Soc. Rev.*, 2021, **50**, 4684–4729.

8 S. Sikarwar, B. C. Yadav, S. Singh, G. I. Dzhardimalieva, S. I. Pomogailo, N. D. Golubeva and A. D. Pomogailo, *Sens. Actuators, B*, 2016, **232**, 283–291.

9 Z. Duan, Y. Jiang and H. Tai, *J. Mater. Chem. C*, 2021, **9**, 14963–14980.

10 Q. Zhao, Z. Yuan, Z. Duan, Y. Jiang, X. Li, Z. Li and H. Tai, *Sens. Actuators, B*, 2019, **289**, 182–185.

11 V. Manikandan, F. Tudorache, I. Petrila, R. S. Mane, V. Kuncser, B. Vasile, D. Morgan, S. Vigneselvan and A. Mirzaei, *J. Magn. Magn. Mater.*, 2019, **474**, 563–569.

12 F. J. Romero, A. Rivadeneyra, A. Salinas-Castillo, A. Ohata, D. P. Morales, M. Becerer and N. Rodriguez, *Sens. Actuators, B*, 2019, **287**, 459–467.

13 H. An, T. Habib, S. Shah, H. Gao, A. Patel, I. Echols, X. Zhao, M. Radovic, M. J. Green and J. L. Lutkenhaus, *ACS Appl. Nano Mater.*, 2019, **2**, 948–955.

14 J. Cui, L. Wang, Y. Han, W. Liu, Z. Li, Z. Guo, Y. Hu, Z. Chang, Q. Yuan and J. Wang, *J. Alloys Compd.*, 2018, **766**, 619–625.

15 S. Jain, S. Chakane, A. B. Samui, V. N. Krishnamurthy and S. V. Bhoraskar, *Sens. Actuators, B*, 2003, **96**, 124–129.

16 D. Lv, W. Shen, W. Chen, R. Tan, L. Xu and W. Song, *Sens. Actuators, B*, 2021, **328**, 129085.

17 Y. Qiu and S. Yang, *Adv. Funct. Mater.*, 2007, **17**, 1345–1352.

18 R. Singh, A. K. Yadav and C. Gautam, *J. Sens. Technol.*, 2011, **1–4**, 9.

19 Z. Duan, Y. Jiang, Q. Zhao, Q. Huang, S. Wang, Y. Zhang, Y. Wu, B. Liu, Y. Zhen and H. Tai, *Sens. Actuators, B*, 2021, **339**, 129884.

20 J. Wang, X.-h. Wang and X.-d. Wang, *Sens. Actuators, B*, 2005, **108**, 445–449.

21 S.-G. Lee, J. Y. Seo, J.-W. Lee, W. B. Park, K.-S. Sohn and M. Pyo, *Sens. Actuators, B*, 2021, **339**, 129928.

22 S. Pathak, K. Jain, P. Kumar, X. Wang and R. P. Pant, *Appl. Energy*, 2019, **239**, 1524–1535.

23 S. Pathak, K. Jain, Noorjahan, V. Kumar and R. P. Pant, *IEEE Sens. J.*, 2017, **17**, 2670–2675.

24 B. C. Yadav, R. C. Yadav, S. Singh, P. K. Dwivedi, H. Ryu and S. Kang, *Opt. Laser Technol.*, 2013, **49**, 68–74.

25 S. Sikarwar and B. C. Yadav, *Sens. Actuators, A*, 2015, **233**, 54–70.

26 B. C. Yadav, A. K. Yadav and A. Kumar, *Int. J. Green Nanotechnol.*, 2012, **4**, 345–353.

27 N. Yadav, P. Chaudhary, K. K. Dey, S. Yadav, B. C. Yadav and R. R. Yadav, *J. Mater. Sci.: Mater. Electron.*, 2020, **31**, 17843–17854.

28 R. J. Si, T. Y. Li, J. Sun, J. Wang, S. T. Wang, G. B. Zhu and C. C. Wang, *J. Mater. Sci.*, 2019, **54**, 14645–14653.

29 A. Erol, S. Okur, B. Comba, Ö. Mermer and M. Ç. Arıkan, *Sens. Actuators, B*, 2010, **145**, 174–180.

30 N. Chaurasiya, U. Kumar, S. Sikarwar, B. C. Yadav and P. K. Yadawa, *Sens. Int.*, 2021, **2**, 100095.

31 A. Farzaneh, A. Mohammadzadeh, M. D. Esrafili and O. Mermer, *Ceram. Int.*, 2019, **45**, 8362–8369.

32 Y. Zhang, Y. Wu, Z. Duan, B. Liu, Q. Zhao, Z. Yuan, S. Li, J. Liang, Y. Jiang and H. Tai, *Appl. Surf. Sci.*, 2022, **585**, 152698.

33 Z. Wang, Y. Xiao, X. Cui, P. Cheng, B. Wang, Y. Gao, X. Li, T. Yang, T. Zhang and G. Lu, *ACS Appl. Mater. Interfaces*, 2014, **6**, 3888–3895.

34 H. Yin, K. Yu, Z. Zhang, M. Zeng, L. Lou and Z. Zhu, *Electroanalysis*, 2011, **23**, 1752–1758.

35 W.-P. Tai and J.-H. Oh, *Sens. Actuators, B*, 2002, **85**, 154–157.

36 M. Bayhan and N. Kavasoğlu, *Sens. Actuators, B*, 2006, **117**, 261–265.

37 S. K. Ganiger and M. V. Murugendrappa, *Polym. Sci., Ser. B*, 2018, **60**, 395–404.

38 M. V. Arularasu, R. Sundaram, C. M. Magdalane, K. Kanimozhi, K. Kasinathan, F. T. Thema, D. Letsholathebe, G. T. Mola and M. Maaza, *J. Nanostruct.*, 2017, **7**, 47–56.

39 S. Borini, R. White, D. Wei, M. Astley, S. Haque, E. Spigone, N. Harris, J. Kivioja and T. Ryhänen, *ACS Nano*, 2013, **7**, 11166–11173.

40 H. Jeong, Y. Noh and D. Lee, *Ceram. Int.*, 2019, **45**, 985–992.

41 N. Marwaha, B. K. Gupta, R. Verma and A. K. Srivastava, *J. Mater. Sci.*, 2017, **52**, 10480–10484.

42 R. Verma, K. K. Naik, J. Gangwar and A. K. Srivastava, *Mater. Chem. Phys.*, 2014, **148**, 1064–1070.

43 Y. Zhang, K. Yu, D. Jiang, Z. Zhu, H. Geng and L. Luo, *Appl. Surf. Sci.*, 2005, **242**, 212–217.

44 R.-J. Wu, Y.-L. Sun, C.-C. Lin, H.-W. Chen and M. Chavali, *Sens. Actuators, B*, 2006, **115**, 198–204.

45 P. V. Shinde, S. Gagare, C. S. Rout and D. J. Late, *RSC Adv.*, 2020, **10**, 29378–29384.

46 E. Singh, U. Kumar, R. Srivastava and B. C. Yadav, *Carbon Lett.*, 2020, **30**, 215–224.

47 R. Verma, A. Awasthi, P. Singh, R. Srivastava, H. Sheng, J. Wen, D. J. Miller and A. K. Srivastava, *J. Colloid Interface Sci.*, 2016, **475**, 82–95.

48 L. Goswami, N. Aggarwal, R. Verma, S. Bishnoi, S. Husale, R. Pandey and G. Gupta, *ACS Appl. Mater. Interfaces*, 2020, **12**, 47038.

49 J. Wang, J. Yang, N. Han, X. Zhou, S. Gong, J. Yang, P. Hu and Y. Chen, *Mater. Des.*, 2017, **121**, 69–76.

50 L. Goswami, N. Aggarwal, M. Singh, R. Verma, P. Vashishtha, S. K. Jain, J. Tawale, R. Pandey and G. Gupta, *ACS Appl. Nano Mater.*, 2020, **3**, 8104–8116.

51 R. Verma, B. Mantri, Ramphal and A. K. Srivastava, *Adv. Mater. Lett*, 2015, **6**(4), 324–333.

52 R. Verma, S. Pathak, A. K. Srivastava, S. Prawer and S. Tomljenovic-Hanic, *J. Alloys Compd.*, 2021, **876**, 160175.

53 S. Pathak, R. Verma, S. Singhal, R. Chaturvedi, P. Kumar, P. Sharma, R. P. Pant and X. Wang, *Sci. Rep.*, 2021, **11**, 3799.

54 P. Kumar, H. Khanduri, S. Pathak, A. Singh, G. A. Basheed and R. P. Pant, *Dalton Trans.*, 2020, **49**, 8672–8683.

55 P. Kumar, S. Pathak, A. Singh, Kuldeep, H. Khanduri, X. Wang, G. A. Basheed and R. P. Pant, *Mater. Chem. Phys.*, 2021, **265**, 124476.

56 A. Singh, S. Pathak, P. Kumar, P. Sharma, A. Rathi, G. A. Basheed, K. K. Maurya and R. P. Pant, *J. Magn. Magn. Mater.*, 2020, **493**, 165737.

57 N. Jahan, S. Pathak, K. Jain and R. P. Pant, *Colloids Surf., A Colloids Surf., A*, 2017, **529**, 88–94.

58 K. Jain, S. Pathak, P. Kumar, A. Singh and R. P. Pant, *J. Magn. Magn. Mater.*, 2019, **475**, 782–786.

59 K. Jain, S. Pathak and R. P. Pant, *RSC Adv.*, 2016, **6**, 70943–70946.

60 P. Kumar, S. Pathak, A. Singh, H. Khanduri, G. A. Basheed, L. Wang and R. P. Pant, *Nanoscale Adv.*, 2020, **2**, 1939–1948.

61 A. Mishra, S. Pathak, P. Kumar, A. Singh, K. Jain, R. Chaturvedi, D. Singh, G. A. Basheed and R. P. Pant, *IEEE Trans. Magn.*, 2019, **55**, 1–7.

62 Noorjahan, G. A. Basheed, K. Jain, S. Pathak and R. P. Pant, *J. Nanosci. Nanotechnol.*, 2018, **18**, 2746–2751.

63 Noorjahan, S. Pathak, K. Jain and R. P. Pant, *Colloids Surf., A Colloids Surf., A*, 2018, **539**, 273–279.

64 Z. Hu, G. Oskam and P. C. Searson, *J. Colloid Interface Sci.*, 2003, **263**, 454–460.

65 Z. Duan, Y. Zhang, Y. Tong, H. Zou, J. Peng and X. Zheng, *J. Electron. Mater.*, 2017, **46**, 6895–6900.

66 M. J. McGrath and C. N. Scanaill, in *Sensor Technologies: Healthcare, Wellness, and Environmental Applications*, Apress, Berkeley, CA, 2013, pp. 15–50, DOI: 10.1007/978-1-4302-6014-1_2.

67 H. Moussa, E. Girot, K. Mozet, H. Alem, G. Medjahdi and R. Schneider, *Appl. Catal., B*, 2016, **185**, 11–21.

68 H. Akazawa, *J. Vac. Sci. Technol., A*, 2021, **39**, 033411.

69 L. Saikia, D. Bhuyan, M. Saikia, B. Malakar, D. K. Dutta and P. Sengupta, *Appl. Catal., A*, 2015, **490**, 42–49.